Journal of Power Sources 233 (2013) 358–368

Contents lists available at SciVerse ScienceDirect

Journal of Power Sources

journal homepage: www.elsevier.com/locate/jpowsour

The influence of porous transport layer modifications on the water management in polymer electrolyte membrane fuel cells

R. Alink [a,*], J. Haußmann [b], H. Markötter [c], M. Schwager [a], I. Manke [c], D. Gerteisen [a]

[a] Fraunhofer ISE, Heidenhofstrasse 2, 79110 Freiburg, Germany
[b] Zentrum für Sonnenenergie- und Wasserstoff-Forschung Baden Württemberg (ZSW), Helmholtzstrasse 8, 89081 Ulm, Germany
[c] Helmholtz Zentrum Berlin (HZB), Hahn-Meitner-Platz 1, 14109 Berlin, Germany

HIGHLIGHTS

- The influence of mechanical/laser perforations and local MPL ablation is analyzed.
- Significant influence on water distribution is found using Synchrotron radiography.
- ESEM water imaging and EDX analysis reveal side-effects due to laser treatment.
- Mechanically locally removed PTLs reveal reduced saturation by drainage effect.
- Improved performance reveals MPL ablations reduce liquid water in CL/MPL interface.

ARTICLE INFO

Article history:
Received 28 September 2012
Received in revised form
28 December 2012
Accepted 16 January 2013
Available online 28 January 2013

Keywords:
PEM fuel cell
Water management
Perforation
Gas diffusion layer
Synchrotron visualization
ESEM

ABSTRACT

In this study, the influence of modifications of the porous transport layer (PTL) on the water management in polymer electrolyte membrane fuel cells is investigated. Laser perforation and milling are used to locally remove either the whole PTL or only the micro porous layer in the PTL. The changed liquid water distribution is visualized using synchrotron radiography and ESEM liquid water imaging. The observed effects are correlated with in-situ performance characteristics, pre-assembly and post-mortem analysis to examine on the beneficial and obstructive effects of the modifications.

The analysis reveals that laser-perforation results in PTFE loss and hydrophilic regions which results in a good performance at dry conditions but serious flooding at high humidification conditions.

Machined perforations show beneficial effects in the in-situ performance characteristics at high humidification conditions. A draining of the vicinity of the perforations is observed which results in an improved oxygen diffusivity. Water balancing and synchrotron visualization indicate that under the analyzed operating conditions the MPL increases the humidification of the ionomer on the one hand but creates an additional diffusion barrier by liquid water in the interface between the cathode catalyst layer and the MPL on the other hand.

© 2013 Elsevier B.V. All rights reserved.

1. Introduction

Water management is of great importance for durability, stability and performance of polymer electrolyte membrane (PEM) fuel cells. A fragile balance between too dry and too wet conditions has to be ensured. On the one hand drying of the membrane results in increased losses due to reduced proton conductivity and a reduced lifetime due to membrane thinning and pinhole formation [1,2]. On the other hand too humid conditions increase losses due to flooding of the oxygen diffusion paths in the porous media or the gas channels. Furthermore, flooding can accelerate degradation of the catalyst layer and the porous transport layer (PTL) due to PTFE loss [3,4] and lead to formation of hot spots due to local reactant starvation.

Great effort has been done in recent years to optimize the water management by redesigning fuel cell components such as the catalyst layer (CLs), PTL and gas distribution plates with respect to their two-phase water transport properties. Due to its position in-between the water generating and water discharging regions in the cell, the 2-phase water transport properties of the PTL play a key role and are therefore subject of several investigations on water management. Nevertheless, the optimization of these layers remains very challenging due to the complex thermodynamics of

* Corresponding author. Tel.: +49 761 4588 5185; fax: +49 761 4588 9320.
E-mail address: Robert.Alink@ise.fraunhofer.de (R. Alink).

0378-7753/$ – see front matter © 2013 Elsevier B.V. All rights reserved.
http://dx.doi.org/10.1016/j.jpowsour.2013.01.085

the capillary pressure driven liquid water transport, the gas diffusion and the phase change within the PTL.

Up to date PTL materials mainly consist of a fibrous substrate (FS) with a defined content of PTFE. Often a micro porous layer (MPL) is attached to the FS on the side toward the CL consisting of a micro-porous structure of carbon and PTFE. The PTFE in both layers increases the hydrophobic effect of the base materials to avoid liquid water accumulation within the pore space. However, also the injection pressure for the liquid product water is increased which results in water accumulation in the interface between the PTL and its place of production in the cathode CL. Although this interface is very sensitive to water accumulations due to the direct blocking of the gas access to diffuse to the active zones, several publications showed that adding PTFE significantly increases the cell performance under humid conditions [5–9].

A promising attempt to support the water management in fuel cells by decreasing the liquid water saturation in the PTL is to create artificial water transport paths by perforation. Laser-perforation seems to be a very attractive method due to its low cost, high accuracy and the good applicability in the industrial fabrication process. In our previous work [10,11], we found that laser-perforating a Toray PTL with holes of a diameter of 80 μm results in a significantly increased fuel cell performance and stability. By dynamic in-situ characterization we could ascribe these improvements to changes in the water transport properties of the porous structure. We theorized that a drainage effect by an in-plane liquid water transport toward the holes is the reason for this improvement.

Due to the diversity of perforation design parameters like diameter, position or shape, optimization of the approach needs a deeper understanding of the mechanisms behind the changes in the complex water management. The water transport is very sensitive on the highly coupled thermodynamics in the fuel cell and modifications for visualizing the liquid water transport will result in changed conditions easily. Experiments using transparent plates [12], fluorescence microscopy [13] and ESEM liquid water imaging [14] revealed important findings but all within their limited area of application. Using synchrotron imaging, the liquid water distribution can be visualized with only little cell modifications [15] and a resolution in the range of 2 μm and a sampling time of 7 s can be achieved easily [16–18].

Neutron imaging has a low sampling rate and spatial resolution but a very high sensitivity to liquid water making cell modifications unnecessary [15,19–21]. Manahan et al. compared the water distribution in cells with perforated PTLs with MPL SGL 10BB obtained by in-situ Neutron imaging under different humidification levels and current densities [20,21]. They found that the saturation in the perforated PTLs is increased up to 46% compared to the unmodified PTL. The analyzed 300 μm holes were cut by laser-perforation and side-effects of the perforation process could have affected the water management. By ESEM and EDX analysis they found that the surrounding of the holes turned hydrophilic and they conclude that PTFE loss during the laser treatment was the reason. They found that the cell performance increased up to a current density of 1.6 A cm^{-2} [20]. At higher currents and with higher humidified inlet gases, the cell performance was lower due to PTL flooding. In Refs. [21,22] the same group found by analyzing the impedance spectra of unperforated and perforated PTLs that the diffusion resistance was decreased at low humidification conditions and increased at high humidification conditions due to the perforations. Probably, the holes remained free of liquid water at low humidification and increased the diffusivity in the PTL due to the direct access of the gases to the active zones. However, if the only beneficial factor is the low diffusion resistance due to the holes, increasing porosity would have the same impact on cell performance.

Just recently, Chen et al. found that perforations in the PTL can help to improve the water transport in the gas channel [23] using modeling. Nishida et al. found that by including grooves into a Toray TGP-H-120 carbon fiber paper, the cell with the grooves exhibits an increased stability during flooding conditions [24]. Knights et al. investigated the influence of perforations with increasing density toward the air outlet in a fuel cell stack [25]. They showed that the perforations increased the power density at high currents significantly.

In this study, we analyze the influence of modifications in carbon paper PTLs (SGL 25BC, SGL 25BA and Toray TGP-H-090) on the fuel cell processes. Besides laser-perforation also mechanical modification is used to avoid side-effects of the laser treatment. Furthermore, both through-holes and only ablating the MPL without damaging the adjacent FS are realized using the mechanical structuring technique.

Due to the complexity of the analyzed topic, we use several characterization techniques to conclude on the influence of the modifications on the water transport by correlating the results. SEM/EDX characterization is used for analyzing the base materials before and after operation in the fuel cell. Changes in the liquid water distribution are visualized by in-situ synchrotron visualization and ex-situ ESEM liquid water experiments. In-situ performance characterization and product water balancing is used to analyze the influence of the modifications on the cell performance and water transport.

Due to the diversity of the used methods, different analytical procedures and setups are used. To structure the numerous diagnostic methods, the results section is subdivided into the examination of the influence of effects by laser-perforation technique and the influence of different modification techniques (laser-perforating, milling, holes, slits). Correspondingly, the influence of the laser-perforation and the general influence of modifications on the water management are discussed separately in the Discussion section.

2. Experimental

In all experiments, Gore™Primea® membrane electrode assemblies (MEAs, membrane thickness: 18 μm, Pt(ca/an): 0.4/0.1 mg cm^{-2}) are used in combination with unmodified SGL 25BC PTLs on the anode side. Only the PTLs on the cathode side are modified and the varying PTLs (SGL 25BC, SGL 25BA and Toray TGP-H-090) and test cells are described in the sections for the different characterization techniques.

2.1. PTL preparation

The laser-perforations are realized using the same technique and hardware as described in our previous work [10,11]. The holes in the PTL are cut by circulating the Nd:YAG laser using a specified radius. Due to the variation of the laser intensity over time, the laser intensity was readjusted for each batch separately such that the desired hole diameter is achieved with minimum intensity. If the PTL has an MPL, the MPL side is always facing the laser beam. The samples are either laser-treated in air atmosphere or argon is blown on the sample by an injector close to the laser head.

Machined slits and holes are realized using a 100 μm drill to investigate the influence of the modification technique. For locally stripping exclusively the approximately 50 μm thick MPL a contact pin with a sharp cone end and a soft spring is used in the CAD milling machine.

In Fig. 1 it is obvious that the applied procedure was successful to solely remove the MPL and the FS is still intact. The width of the machined modifications are in the range of 130 μm.

2.2. Synchrotron radiography

Synchrotron radiography measurements were carried out throughout two separate beam-times at the BESSY II electron storage ring at the Helmholtz-Zentrum Berlin (BAMline), Germany [26,27]. The experimental setup at the beam-line has already been reported in our previous paper [28]. The spatial resolution is 2.17 μm pixel^{-1} and the temporal resolution is 7 s image^{-1} in beam-time 1, 5 and 10 s image^{-1} for the through-plane (TP) and in-plane (IP) visualization in beam-time 2 respectively. The examined materials and characteristics of the test-cells are summarized in Table 1, all laser perforated PTLs are laser perforated in argon atmosphere. In the first beam-time (cell 1), only laser perforated PTLs are examined, in the second beam-time (cell 2) the modification technique is varied.

In cell 1, 4 visualization fields are drilled into the end plates [28] and the PTL under each visualization field is perforated with a different perforation diameter. The gap distance of the perforations is 0.8 mm and at least one perforation row is beneath the land and one is beneath the channel in each visualization field. To investigate the influence of the presence of the MPL, a SGL 25BC PTL is compared to a SGL 25BA which is the FS of the SGL 25BC PTL. Since our former work [10,11] was focused on the influence of perforating a Toray paper PTL, we also used the same material in this work again.

The influence of different modification techniques (milling, laser perforation, slits and holes) in a SGL 25BC PTL is analyzed in beam-time 2. A separate cell (cell 2 in Table 1) is used which enables both the visualization in the IP and the TP direction. Both in the IP and TP direction, 4 channels are in the visualization field. The modifications are placed under the channel only with a gap distance of 2 mm along the channel, the slits have the same length as the channel width (1 mm).

Throughout the whole experiments, the gas flow is set to a constant flow rate on the cathode side (air) and on the anode side (hydrogen or nitrogen), corresponding to a stoichiometric ratio of 2.5 on the cathode side and 1.4 on the anode side at 1 A cm^{-2}. The cell temperature is controlled to 55 °C by a liquid coolant loop. For each sequence, the cell is dried by purging with dry air on the cathode side and dry nitrogen on the anode side for 15 min. Then the gas supply is switched to air and hydrogen with a relative humidity (RH) of 0.75 respectively. The cell is allowed to equilibrate for another 10 min before the load is set to 1 A cm^{-2}. Due to the water production by the electrochemical reaction and the long gas path from the air inlets, the air in the visualized area is always over-humidified.

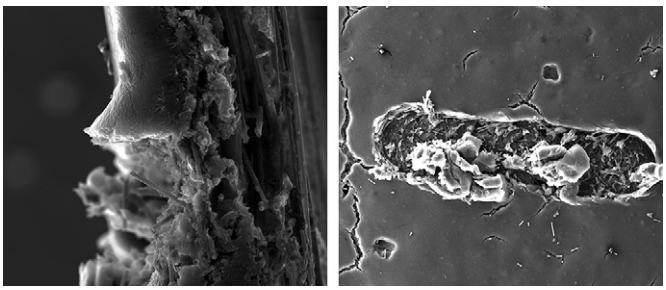


Fig. 1. SEM cross section (left, MPL side is on the left hand side) and top view (right, MPL side is visible) of a PTL with the locally removed MPL.

Table 1
Characteristics of the two test cells used for the synchrotron visualization experiments. All laser-perforated PTLs are laser perforated in argon atmosphere.

	Cell 1	Cell 2
Active area	10 × 10 cm^2	44 mm^2
Land width	1 mm	0.5 mm
Channel area	1 mm^2	0.8 mm^2
Visualization field TP	d = 10 mm (4×)	13 × 3.5 mm
Visualization field IP	–	10 mm
Cathode PTL	SGL 25BA SGL 25BC TGP-H-090	SGL 25BC
Modifications	Laser: holes PTL d = 80, 100, 120,180 μm	Laser: holes PTL (150 μm) milled: holes PTL (130 μm) slits PTL (130 μm) slits MPL (130 μm)
Modification pattern	Square pattern 0.8 mm under channel/land	Gap distance 0.8 mm under channel

2.3. In-situ performance characterization

For investigating the influence of different manufacturing techniques (milling/laser ablating, slits/holes) and the laser parameters (hole diameter and substrate material), different test cells and protocols are used which are described in the following subsections.

2.3.1. Examination of the influence of laser-perforation

To characterize the influence of different laser-perforating techniques on the cell performance, variously laser-perforated SGL 25BC PTL segments (hole diameter 80 μm and 120 μm, perforated in argon or air) are distributed over the active area in a 4 × 4 segmented test cell. The used segmented fuel cell hardware has been described previously [29]. Fig. 2 shows the segmented gas distribution plate and 11 of the total 16 differently modified PTL 1.76 × 1.76 cm^2 segments. An electrically isolating mask is used to fix the PTLs with respect to the gas distribution plate. The 50-channel impedance test bench as described in our previous work [30,31] is used for spatially resolved characterization. Each perforation technique is realized within two PTLs and unmodified PTLs

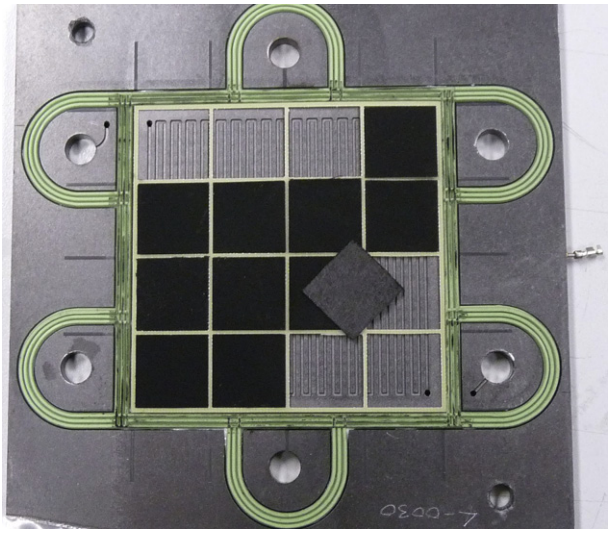


Fig. 2. Segmented test cell used for the in-situ performance characterization of the laser-perforation technique. Shown is the segmented gas distribution plate and 11 of total 16 differently modified PTL segments which are fixed using an isolating mask.

are placed in between the perforated PTLs for comparison. The gap distance of the laser-perforations is 0.8 mm in each direction such that the holes are both present under the land and the channel. The stoichiometric ratio is kept constant at 1.5 on the anode and 2 on the cathode side. Gases are humidified using membrane humidifiers to $RH = 0.32$ and the cell temperature is kept constant at 40 °C.

2.3.2. Examination of the influence of different modification techniques

For the characterization of the influence of different modification techniques, a test cell from Baltic fuel cells (qCF FC 25/100 LC) with a 5-fold serpentine flow field and an active area of 5×5 cm^2 is used. The channel and land width is 1 mm respectively, the slits and holes are placed under the channel only. The modifications have a gap distance of 0.8 mm along the channel and the slits have the same length as the channel width (1 mm). The experimental conditions are summarized in Table 2. Table 2 also gives a rough estimation of the fraction of the channel length where the water content in the gas reaches saturation $L_{RH=1}$ according to:

$$L_{\mathrm{RH}=1} = \frac{m_{\mathrm{RH}=1} - m_{\mathrm{H_2O,in}}}{m_{\mathrm{H_2O,out}} - m_{\mathrm{H_2O,in}}} \quad (1)$$

with $m_{\mathrm{RH}=1}$ as the absolute humidity at saturation pressure and $m_{\mathrm{H_2O,out}}$, $m_{\mathrm{H_2O,in}}$ as the absolute humidity at the outlet and inlet. $m_{\mathrm{H_2O,out}}$ and $m_{\mathrm{H_2O,in}}$ are determined by condensing the outlet water with and without running the fuel cell using an unmodified PTL. The cells are characterized near the limiting current due to the maximum impact of mass transport limitations. Three different cathode gas humidification conditions (dry (dry), humidified (hum) and over-humidified (ohum)) are applied while the RH on the anode side is always 0.65. Each set-point is kept constant for 4 h respectively while the mass flows are set to 4 l min^{-1} on the cathode and 1 l min^{-1} on the anode side. The cell temperature is controlled to 50 °C. For the over-humidified conditions, the water flow of the steam injector humidifiers are chosen two times higher than the flow at $RH = 1$.

During the 4 h of characterization, the product water is collected on the cathode and anode outlets separately using condensers. Prior to the characterization the cell is allowed to equilibrate for 30 min, then the condensers are cleared.

2.4. Ex-situ analysis

An ESEM (FEI Quanta 400) with an EDX (EDAX) is used to analyze the surface structure and element composition of the MEA and PTL materials. For the ESEM liquid water transport visualization the same experimental protocol as described in our previous paper [14] is used. By applying a temperature gradient over the thickness of the PTL, liquid water is condensed only at the bottom of the PTL. The liquid water accumulates and the breakthrough to the PTL surface due to the pressure buildup is visualized by the SEM.

Table 2
Test-settings for the in-situ characterization of the different perforation manufacturing techniques.

	λ		I (A cm^{-2})	RH_{inlet}		L_{RH}=1	
	an	ca		an	ca	an	ca
Dry	3.1	5.6	1.7	0.65	0	3.4	1.8
Hum	3.1	5.2	1.8	0.65	0.73	0.6	0.4
Ohum	3.3	5.2	1.8	0.65	>1	0.3	−1.7

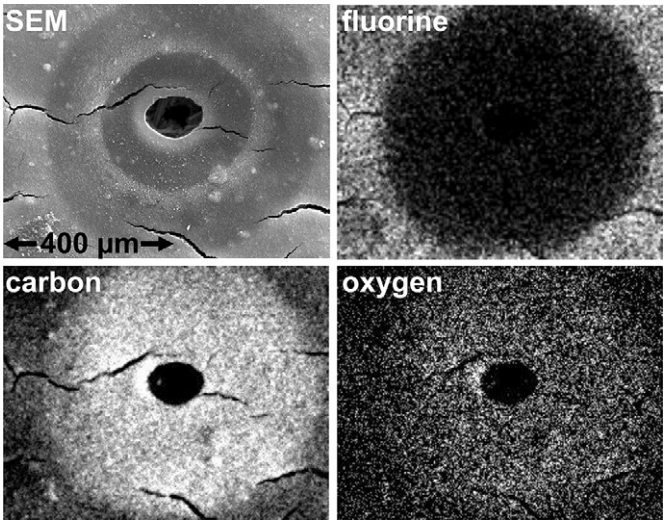


Fig. 3. SEM image and the distribution of carbon, oxygen and fluorine (light colors correspond to high concentrations) of the surface of the MPL side after the laser treatment before operation in a fuel cell. The sample was laser-treated in argon atmosphere.

3. Results

3.1. Influence of laser-perforation

3.1.1. Pre-assembly analysis

Fig. 3 shows a SEM image and the corresponding distribution of carbon, oxygen and fluorine near a laser-perforated region on the MPL side of the PTL. In agreement with Manahan et al. [20,21], the laser-perforation significantly reduced the content of fluorine around the hole. Furthermore, the concentration of carbon and oxygen increased. The same distribution was observed on the FS side of the PTL (not shown). In Fig. 4(a), ESEM water transport experiments show that the water is first visible in the vicinity of the perforation before it is visible in the hole itself. Due to the hydrophilic wetting of PTL material surrounding the hole, the water at the bottom of the PTL is wicked and transported to the surface immediately. This behavior is observed only in the sequences with the PTLs perforated in air atmosphere. However, the PTLs showed varying behavior and most of the perforations remained hydrophobic. In Fig. 4(b), the round shape of the droplets in the hole and the fact that the water reaches the PTL surface in the hole first, indicates that the PTL material that was perforated in argon atmosphere still is hydrophobic.

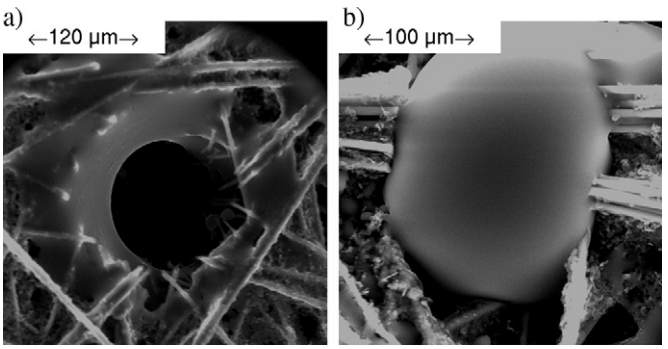


Fig. 4. ESEM liquid water breakthrough visualization of a laser-perforated PTL exhibiting hydrophilic (a) and hydrophobic (b) wetting properties of the area surrounding the holes, reprinted from Ref. [14].

3.1.2. Performance characterization

In Fig. 5 the performance of differently laser perforated SGL 25BC PTLs and their respective neighboring, unperforated PTLs with the same distance to the air inlet along the gas channel are compared. Therefore, the difference between the current production of the perforated segments and the unperforated segments $\Delta I = I_{perforated} - I_{unperforated}$ at 0.4 V is shown.

Only the PTLs perforated in argon atmosphere with a diameter of 80 μm exhibit an improved performance compared to the unperforated PTLs, while the PTLs with the wider holes (120 μm) show a decreased performance. The PTLs perforated in air atmosphere show a lower performance than the unperforated PTLs and the PTLs perforated in argon atmosphere. The segments perforated in air atmosphere with the smaller diameter (80 μm) show a significantly decreased performance.

After disassembling, the PTLs are characterized for their elemental composition by means of EDX. Fig. 6 (left) shows the fluorine content of the segments over a scanning area of 3.4 mm^2 respectively which is a measure for the PTFE content. The fluorine content of the perforated PTLs is less than half of the content in the unperforated segments. The segments perforated in air atmosphere with the small diameter (80 μm) show nearly a complete PTFE loss which is consistent with the low performance of these segments in Fig. 5. In Fig. 6 (right) a small water droplet is placed on the surface of the PTLs and the surface wetting of these segments (segments 9 and 10) turned hydrophilic while the others remained hydrophobic.

3.1.3. In-situ X-ray liquid water visualization

Fig. 7 shows a synchrotron visualization of a Toray TGP-H-090 PTL 180 s after applying the load. The influence of the perforations on the liquid water distribution is very pronounced and many

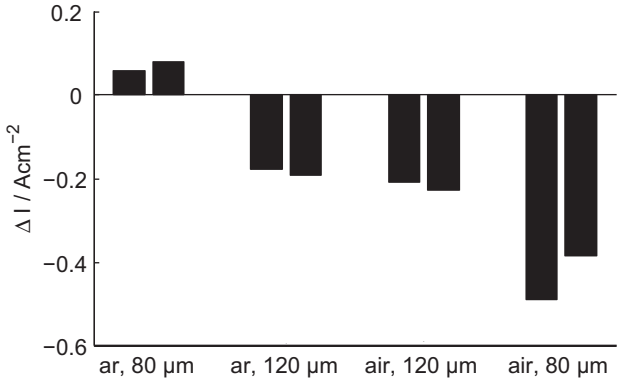


Fig. 5. Performance characteristics at 0.4 V of the segments having differently perforated SGL 25BC PTLs within the segmented cell. The current of the modified PTL segments is subtracted from the respective neighboring, untreated segment.

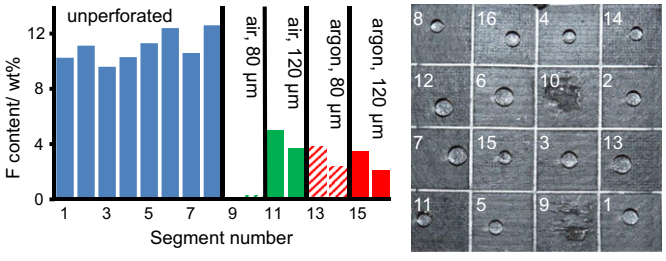


Fig. 6. Fluorine content of the surface of all PTLs according to EDX analysis (left) and photograph of the segmented cell (right, FS side of the PTLs is visible) after disassembling. A small water droplet is placed on top of the FSs to visualize the surface wetting of the FSs.

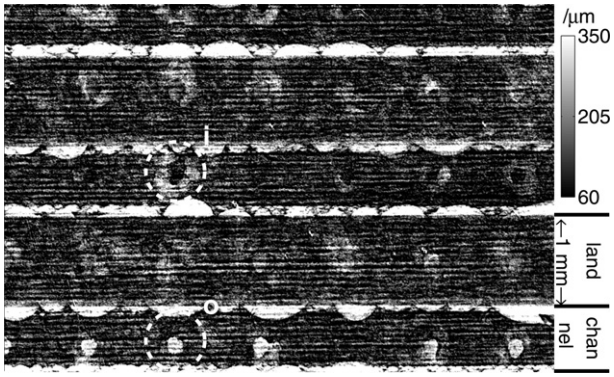


Fig. 7. Water thickness distribution in a cell with a perforated Toray TGP-H-090 PTL (d_{hole} = 180 μm), 180 s after the current step.

of the perforations are visible, independent on their position under the land or the channel. However, most of the holes are visible by the liquid water surrounding the holes (feature i) suggesting hydrophilic wetting while only few exhibit hydrophobic wetting (feature o). The inside of the hydrophilic holes fill with liquid water only after the vicinity is already fully saturated or if they are filled up by a droplet moving in the gas channel.

The liquid water distribution for the SGL 25BC PTL in Fig. 8 is different. Besides the lower overall water thickness due to the PTFE in the PTL, most of the holes are visible but with a hydrophobic wetting (feature o). In the bottom channel, liquid water features (feature f) are forming around the perforations in the channel regions. The shape of the features and the fact that they are exclusively present at the place of the perforations in the cathode channel suggests that a water film is forming between the PTL surface and the channel walls. These water formations are only found for the SGL 25BC PTL and they disappeared when a liquid water drop was moving through the channel.

Furthermore, droplets preferably appear on the channel walls exactly at the position where perforations are present under the land (feature d). In Fig. 9 the filling of the perforation under the land and the evolution of the corresponding droplet on the channel wall in feature d is shown. 84 s after the current step, the hole under the land is filled with liquid water. A liquid water branch is forming between the perforation and the channel subsequently within 14 s. When the channel is reached, the branch remains stable and the droplet grows on the channel wall.

In Fig. 10 the mean steady state water thickness in the TP direction is plotted against the distance to the hole center. For the calculation, the average water thickness of a 70 s time span is

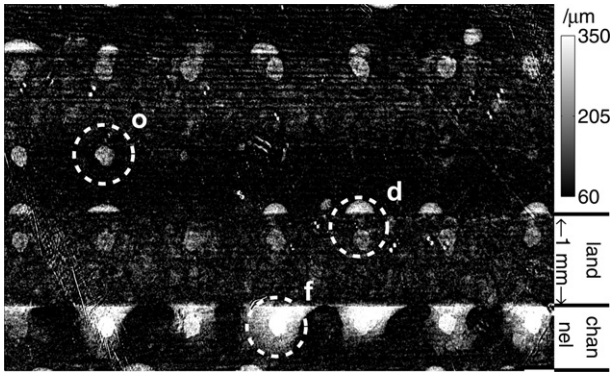


Fig. 8. Water thickness distribution in a cell with a perforated SGL 25BC PTL (d_{hole} = 180 μm), 300 s after the current step.

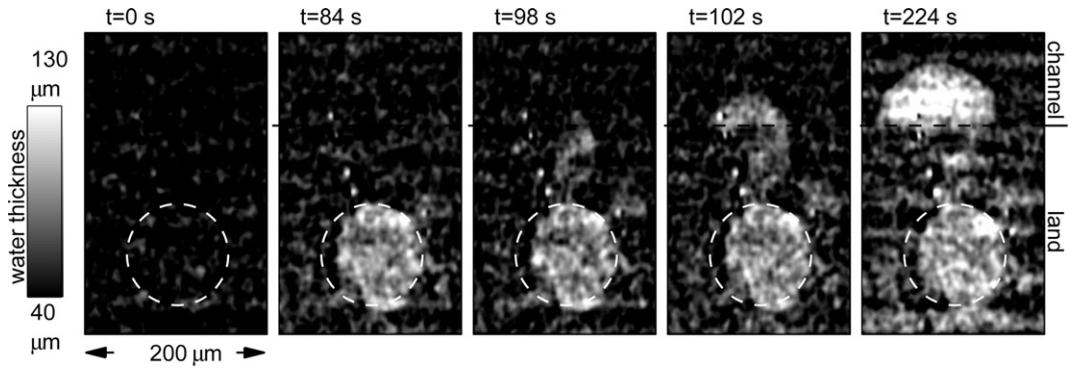


Fig. 9. Filling of a hole under the land (feature d in Fig. 8) after the load was stepped from 0 A cm^{-2} to 1 A cm^{-2} and water path formation into the channel.

calculated, at least 350 s after the current step. The profiles are obtained over a rectangular area ($l = 80$ µm, $b = 800$ µm) centered over the hole, with the long side aligned with the direction of the channel. Due to the varying characteristics of the perforations, the water thickness profiles are averaged over a number of equal perforations. The shown profiles contain both the profiles of the holes under the land and the channel since there is no obvious difference in the characteristics. Holes which were not visible, close to the channel/land interface or close to regions with high water accumulations not attributed to the perforations are not taken into account.

Regarding the difference between the water thickness in the center and at 400 µm distance, the drilled holes are fully filled with liquid water and droplets are forming on the hole surface. However, temporal fluctuations by the droplet formation may contribute to the high standard deviations for all profiles.

Only the PTLs with MPL (SGL 25BC) exhibit a sharp decrease of the saturation in the region of the edge of the holes (80 µm) indicating that the holes are filled with water and the surrounding PTL structure is still hydrophobic. The sharp decrease is not visible for the PTLs without MPL (Toray TGP-H-090 and SGL 25BA) due to a mixed behavior of the holes. This is consistent with the findings in Fig. 7 where many of the holes in the Toray paper PTL turned hydrophilic (feature i) while others remained hydrophobic (feature o).

The PTL saturation toward the edge of the hole compared to the saturation at 400 µm is significantly decreased only for PTLs in beam-time 2. The profile around the laser perforated holes in beam-time 2 is almost identical with the profile around the drilled holes indicating a low influence of the laser treatment on the PTL wetting.

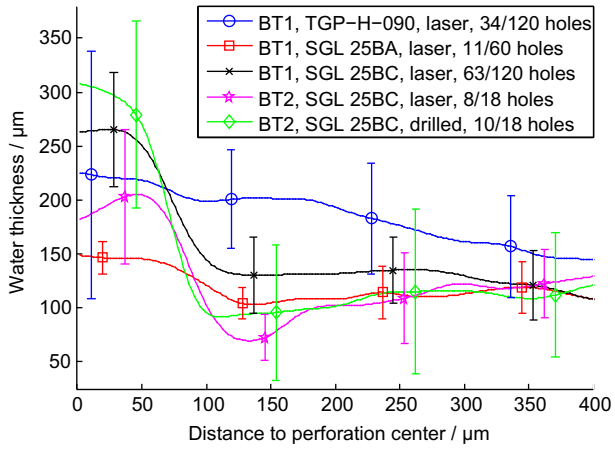


Fig. 10. Average TP liquid water thickness, dependent on the distance to the hole center for three different types of PTL and for beam-time 1 (BT1, $d_{hole} = 180$ µm) and beam-time 2 (BT2, $d_{hole} = 150$ µm) and the number of holes that could be used for the calculation.

3.2. Influence of different modification techniques

3.2.1. Performance characterization

Fig. 11 shows the results of the galvanostatic performance characterization and water balancing of the cells with the different PTL modifications. Shown is the cell voltage, high frequency resistance (HFR, measured at 10 kHz) and ratio of the product water that was collected in the cathode exhaust gas ($X_{H_2O,cathode}$) using dry, humidified and over-humidified cathode inlet gases.

In general, the HFR and ($X_{H_2O,cathode}$) show a strong correlation due to the coupling by the MEA humidification. High MEA humidification results in a high MEA protonic conductivity but also in a high water desorption rate in the anode electrode. The high desorption must be balanced by a high diffusive water flux from the cathode to the anode side through the ionomer leading to a decreased ($X_{H_2O,cathode}$). In contrast, the product water ratio on the cathode side is the lowest for the unperforated PTL whereby the HFR is higher than the HFR of the PTL with removed MPL.

At dry conditions, the PTL with the removed MPL shows the best performance which is attributed to the high membrane humidification, obvious by the low HFR and low product water ratio on the cathode side. Even though having the same perforation structure, the laser-perforated holes show a significantly lower HFR than the drilled holes indicating a higher MEA humidification. However, with higher humidification it suffers from flooding. At over-humidified conditions it could therefore not be operated at the predefined current anymore and the data points for the HFR and ($X_{H_2O,cathode}$) are determined at a slightly lower current (1.6 A cm^{-2}) than the other cells (1.7 A cm^{-2}). Both values show a very well humidified membrane and the highest water crossover to the anode side. At over-humidified conditions all other modifications show almost the same performance, while the unmodified PTL exhibits an approximately 30 mV lower cell voltage.

Fig. 12 shows SEM top-views and cross section views of PTLs and MEAs after the in-situ performance characterization. The top views of a drilled hole (a and b) show that the holes in the PTL remained stable throughout the experiments. Furthermore, a significant impact of the perforation on the MEA structure is visible in the top-view of the electrode surface (c) and the cross section view (d) through the PTL/MEA sandwich. The thickness of the MEA and the catalyst layer on the cathode side seem to be increased. Also, the anode catalyst layer partly lost contact to the MPL in the place of the perforation.

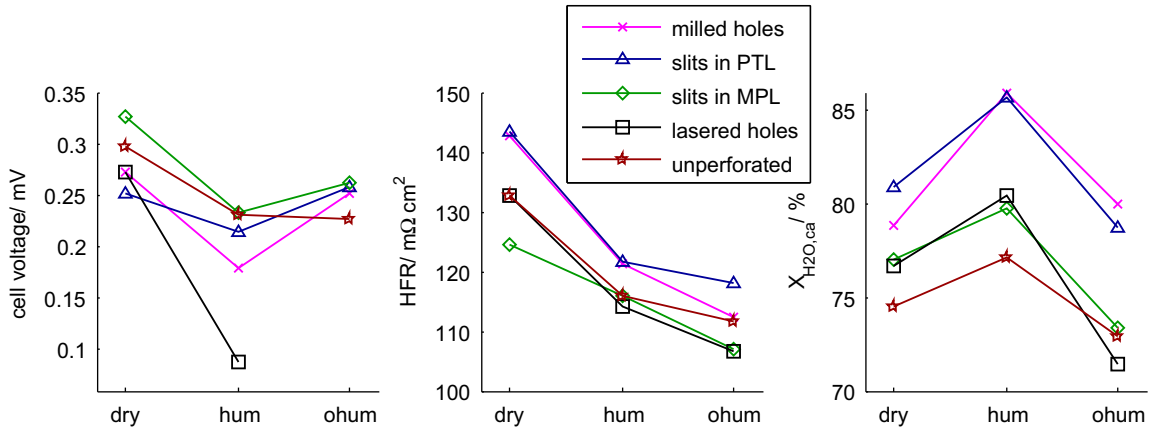


Fig. 11. Cell voltage, HFR and ratio of product water on the cathode side at three different cathode humidification scenarios. Note that the cell currents for the humidified and over-humidified case is 1.8 A cm^{-2} and 1.7 A cm^{-2} for the dry case.

3.2.2. *In-situ X-ray liquid water visualization*

Fig. 13 shows the IP and TP water thickness profiles of the SGL 25BC PTLs modified with a 130 μm slit in the channel. The shown profiles are calculated using steady state sequences (Section 3.1.3) and subsequent averaging over all profiles with the same kind of modification. To analyze the influence of the modifications on the adjacent regions, the profiles are extracted both centered over the modifications and directly beneath the perforations with a center to center gap distance of 100 μm. Furthermore, profiles in between two modifications are extracted to obtain the profile of an unmodified region. Here, the distance to the modification is 1 mm respectively and the influence on the water distribution is assumed to be negligible.

In the IP direction, the highest water saturation in the FS, MPL and MEA is found for the removed MPL. Despite the modifications are only realized on the cathode side, also the water content in the anode PTL is the highest here. The water thickness beneath the removed MPL is still higher than in the unperforated region both in the IP and TP direction.

Both in the IP and TP direction the saturation in the regions where the whole PTL is removed is lower than where only the MPL is removed but higher than in the unperforated regions. Obviously, only a fraction of the slits fill with the liquid water. In the TP images (not shown), the high saturation in the places with the removed MPL is continuous over the hole length of the slits indicating that the whole cavity is filled with water. In contrast, only confined places with high water content are visible in the places where the whole PTL was removed. Apparently, the liquid water forms droplets or confined water paths through the slits if the whole PTL is removed but fills the whole slit if only the MPL is removed.

In the cathode channel, the droplet formation is higher in the places of both modifications, indicating an increasing water flux from the MEA through the modifications. The water content in the channel beneath the removed MPL is still high but beneath the removed PTL it is the same as in the unperforated region.

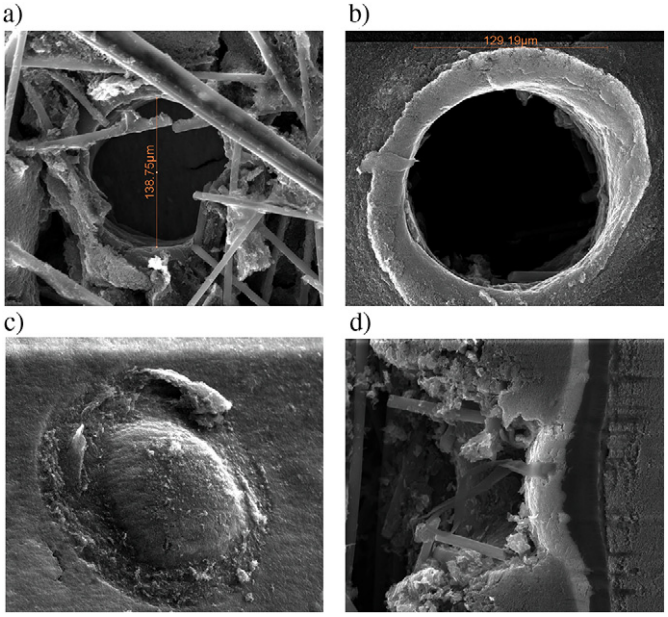


Fig. 12. SEM top views of the FS side of the PTL (a), the MPL side of the PTL (b) and the MEA surface (c) as well as a cross section view of the MEA and PTL sandwich (d, anode is on the right hand side) in the place of a drilled hole after operation in a fuel cell. The edge length of the images is 200 μm.

4. Discussion

In this section the side-effects of the PTL laser-perforation are discussed, before the influence of the modifications on the water management is discussed. Fig. 14 shows a schematic of the proposed water management scenarios for the different PTL modifications, discussed in the following subsections.

4.1. *Side-effects of the laser-perforation technique*

Different results clearly show that the laser-perforation changes the wetting of the vicinity of the perforations toward hydrophilic. The hydrophilic wetting is observed both in the ex-situ ESEM visualization experiments in Fig. 4 and in the in-situ synchrotron visualizations in Fig. 7 (feature i). In the performance characterization experiments in Figs. 5 and 11 the cells with laser-perforated PTLs show a significantly reduced performance under flooding conditions. This confirms the findings by Manahan et al. [20,21] where they could attribute the decreased performance of the perforated PTLs to a high water content in the cathode PTL at flooding conditions. EDX mappings in Fig. 3 show that the elemental composition of the hole vicinity has been changed due to laser perforation and the round shapes of the changes indicate that temperature effects are the reason. A change in the PTFE content or structure due to the high temperatures is very likely.

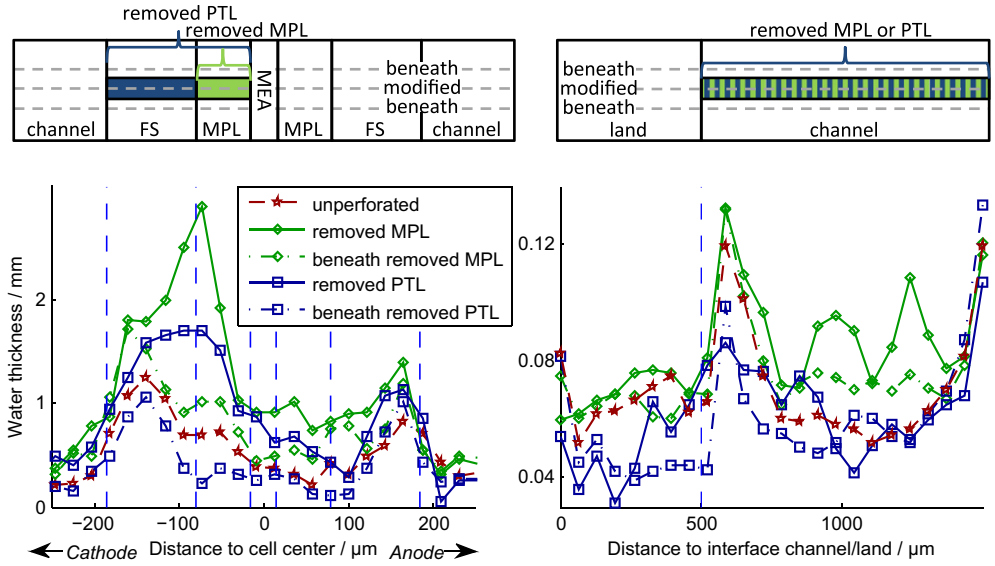


Fig. 13. IP (left) and TP (right) liquid water thickness in the place of the modifications and directly beneath the modifications in a SGL 25BC PTL. The region between the modifications is labeled as unperforated.

However, PTFE loss alone can not explain the wetting properties to change to hydrophilic. The contact angle of the fiber substrate is higher than 90° [32] and hydrophilic regions are also observed for the Toray paper PTL with no PTFE. A restructuring of the graphite surface or an oxide layer on the fibers caused by the high temperatures can be explanations. The increased oxygen content around the hole in Fig. 3 can be due to the adsorbed oxygen on the carbon fibers causing them to turn hydrophilic [33].

In the ESEM experiments (Section 3.1.1) the hydrophilic regions are observed only with the PTLs laser-perforated in air atmosphere. For perforating in air atmosphere, smaller radii had to be chosen to obtain the same perforation diameter most likely due to glowing of the fibers in the presence of oxygen. In argon atmosphere the glowing was mostly prevented. Corresponding results were found in the in-situ experiments in Figs. 5 and 6. The two segments that were laser-perforated in air atmosphere suffered significantly from flooding due to hydrophilic PTLs. The PTLs perforated with the same diameter in argon atmosphere show even an improved performance indicating that the argon successfully prevented the formation of the hydrophilic regions.

However, in the synchrotron visualization experiments (Section 3.1.3) the hydrophilic wetting is also observed for the PTLs treated in argon atmosphere. Even though the same materials were perforated using the same setup and technique, the water thickness profiles in

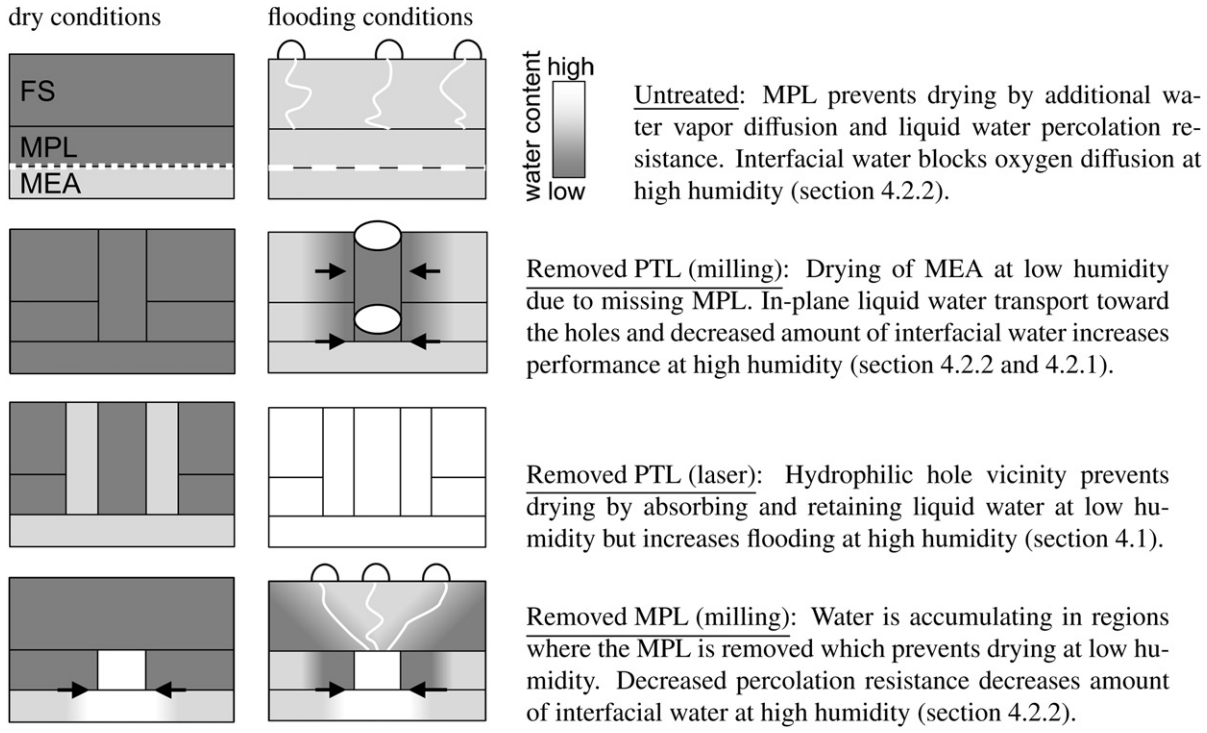


Fig. 14. Conclusion on the influence of the PTL modifications on the liquid water distribution at drying and high humidification conditions.

Fig. 10 for beam-time 1 and beam-time 2 and the ESEM liquid water visualizations described in Section 3.1.1 show varying characteristics. Hydrophilic wetting was only observed for the PTLs in beam-time 1 and desired effects like the drainage effects (discussed in Section 4.2.1) could only be observed for the PTLs in beam-time 2. Accordingly, the formation of the hydrophilic regions appears to be very sensitive to variations in the perforation process. The laser intensity was adjusted for each batch separately using the same procedure and variations were also observed within different holes of the same batch. Reasons could be that the absorbed amount of energy varies due to inhomogeneous PTL properties, fluctuations in the laser intensity or variations in the position of the PTL with respect to the laser. Furthermore, different laser exposure times during circulating the laser for preparing the different perforation diameters could have caused different cell performances in Fig. 5.

In Fig. 10 the profiles of the two PTLs without MPL are similar, even though compared to the SGL 25BA the Toray paper PTL is stiffer, thicker (280 μm compared to 190 μm) and not treated with PTFE. Since the hydrophilic wetting is observed more often for these PTLs, the presence of the MPL obviously suppresses the mixed wetting behavior.

4.2. Influence of modifications on the water management

The influence of the perforations on the water distribution can be manifold. Most likely, the changed capillary pressure distribution plays a key role for the perforation approach. According to the Young–Laplace equation:

$$p_c = -2\gamma\frac{\cos(\phi)}{r} \quad (2)$$

the capillary pressure p_c for a cylindrical pore with contact angle ϕ is inverse proportional to the pore radius r (with γ as the surface tension of water). Fig. A.15 shows the capillary pressure in the MPL and FS and the temperature lift due to ohmic and reaction heating according to a simple thermal model (Appendix A) for different perforation diameters. Compared to the capillary pressure of the mean pore diameter in the FS and the maximum width of the natural cracks in the MPL (10 μm [34,35]), the capillary pressure change is insignificant for diameters larger than 100 μm. However, the temperature lift is rapidly increasing in holes bigger than 100 μm which can be significant for the water management due to the high sensitivity of the thermodynamics on temperature effects. Thus, further increasing the diameter of the hole results in undesirable effects like reduced PTL electrical conductivity, shear stress for the MEA due to the locally missing counter pressure and local hot-spots. Fig. 12 shows deformations in the structure of the MEA with the 130 μm slits after in-situ testing, which can lead to membrane failure after longer operation.

In the following subsections, the influence of the modifications on the water management is discussed. Since the beneficial effects of the perforation approach is ascribed to the IP water transport toward the modifications [10,11,14], this effect is discussed separately from the general influence of the modifications on the water transport.

4.2.1. In-plane liquid water transport

The most evident explanation for beneficial effects by perforation is that the water collects in the perforations by a drainage effect which reduces the saturation in the vicinity of the holes. The water that is built in the regions besides the perforations travels IP toward the hole where it is transported to the channel. This drainage is supported by the anisotropic fiber orientation in the PTL since the pressure for pushing the water in the IP direction is lower than for the TP direction. In the presented results we found several indications for the presence of this mechanism which are described in the following.

1. In the synchrotron visualization in Fig. 8 (feature d), droplets at the channel wall are forming at the places of the perforations under the land. The sequence in Fig. 9 shows that the droplets are fed by the perforations under the land. Most likely, the electrode under the water filled hole does not produce any water since the oxygen path to the active sites is blocked. Consequently, the liquid water feeding the droplets must originate from the surrounding regions, following the IP capillary pressure gradient toward the hole.
2. Both in the TP and IP water thickness profiles in Fig. 13, the liquid water saturation besides the slits in the PTL is lower than in the unperforated regions. This effect is also very pronounced in the regions under the land where the product water must travel IP to fill the perforations in the channel. In the IP visualization, the droplet formation in the channel above the perforations is increased by a high water expel rate.
3. In Fig. 10 the saturation in the PTL is lower for a lower distance to the hole edge for the mechanically perforated PTL due to a decreasing impact of the drainage effect with an increasing distance to the hole.
4. In the ESEM liquid water visualizations of a hydrophobic PTL in Fig. 4, the liquid water reaches the surface of the PTL in the hole first. Even though the void volume in the hole is approximately 30% higher than in the porous structure of the PTL, the hole is filled with liquid water before the breakthrough through the surrounding surface is observed.

4.2.2. Influence of modifications on the water management

4.2.2.1. Effects at dry conditions. In Fig. 11 at dry conditions, the PTL with the removed MPL shows the best performance while the HFR and ($X_{H_2O,cathode}$) are low due to a high MEA humidification and high protonic conductivity of the MEA. This is consistent with the synchrotron visualizations in Fig. 13 where also an increased MEA humidification is found for the MEA with the removed MPL. The accumulating water in the regions where the MPL is removed is in direct contact with the MEA leading to maximum ionomer humidification. In contrast, an increased MEA drying can be observed for the cells with the milled holes and milled slits. The product water can directly be transported to the channel in the vapor form if no additional diffusion resistance by the FS is present.

The MEA humidification with the laser-perforated PTLs is higher than with the mechanically perforated PTLs. Obviously, the hydrophilic regions around the holes improve the water retention capability of the PTL at dry conditions by adsorbing the liquid water. Anyway, even though the HFR is lower, the cell performance is not increased. Mass transport losses due to the liquid water filled structure are most likely already present at the low humidification levels.

In the cell with the unperforated PTLs the MPL successfully retains the water at dry conditions resulting in a low HFR and high water crossover to the anode side. Accordingly, in the mechanically modified PTLs the missing MPL results in a higher water expel rate on the cathode side and a low HFR. Due to the direct path from the electrodes to the channel, more product water is expelled over the cathode gases.

4.2.2.2. Effects at wet conditions. The found influences of the modifications on the liquid water transport are manifold. In Fig. 8, the perforations are clearly visible and liquid water features are forming in the channel (feature f). These features are most likely thin film formations on the PTL surface. The films are only observed in the vicinity of the laser-perforated holes and appear irregularly and disappear if a water droplet is passing the channel.

Despite the significantly changed liquid water distribution, all other perforation techniques show a rather low influence on the cell performance in Fig. 11. Even though 2% (holes) or 17% (slits) of the PTL structure was removed, still the cell voltage at flooding conditions is 30 mV higher than for the untreated PTLs.

When changing from humidified to over-humidified conditions in Fig. 11, the performance of all cells increases except for the cell with the unperforated PTL. Even though the RH is already high (0.73) at the air inlet and $RH = 1$ is reached at 40% of the channel length (Table 2), the MEA water content of the modified PTLs is still increased when changing to even higher humidification. However, the HFR of the unperforated cell remains constant while more product water is expelled on the anode side. At over-humidified conditions ($X_{H_2O,cathode}$) is on a low level, while the HFR is high. Accordingly, other effects than the MEA humidification may influence the HFR. A possible explanation is an increasing amount of liquid water in the interface CL/MPL, creating an additional contact resistance. The high entry pressure for the liquid water to enter a natural MPL crack (13 kPa, Fig. A.15) results in a high MEA humidification on the one hand but in an increasing amount of interfacial water. The modifications prevent this interfacial water at flooding conditions but also decrease the MEA water content at dry conditions. However, in the synchrotron visualization in Fig. 13 the interfacial water is not visible, most likely because the film-thickness is below the resolution of the imaging.

The IP and TP water thickness profiles in the synchrotron visualizations in Fig. 13 show that the saturation in the regions where only the MPL is removed is higher than where also the FS is removed. The water from the surroundings of the modifications is most likely collecting in the void space in the MPL until the pressure is high enough to push through the FS. Since in Fig. 13 the droplet formation in the channel above the modifications is high, the flux of liquid water through the modified regions must be increased. The additional water is not due to the IP water transport toward the modifications in the FS since this effect is not observed for the PTLs with the removed MPL (as discussed in Section 4.2.1). However, the drainage effect in the FS for the through holes obviously does not have a mayor effect on the oxygen diffusivity since the performance is not higher for the through holes. Therefore, the mayor reason for the improved performance of the mechanical modifications is most likely not the drainage in the FS. Rather, drainage of the interfacial water between the catalyst layer and the MPL could result in the improved performance and the increased droplet formation in the channel above the removed MPL.

The increased droplet formation is not confined to the regions directly above the modifications as observed for the through-holes. Due to a fan-shaped spreading of the liquid water from the modification to the PTL surface (Fig. 14) the increased water saturation is also visible in the regions next to the modifications.

In recent publications, the advantage of the application of an MPL in addition to a FS is attributed to the presence of cracks or defects in the MPL material [35,36]. Water travels preferably through the cracks toward the FS, bypassing the large water pressure necessary to penetrate into the small hydrophobic pores in the MPL bulk material. As a result the number of breakthrough paths in the FS is reduced. The interpretation of the presented results supports this theory. Furthermore, the natural cracks in the MPL may also drain the liquid water in the interface and contribute to the beneficial effect of the MPL.

5. Conclusions

The influence of both mechanical and laser perforating different PTL materials on the water management is analyzed using different experimental techniques. In-situ synchrotron radiography, performance characterization and water balancing and ex-situ ESEM liquid water visualization and SEM/EDX analysis are correlated to conclude on the water transport mechanisms in the fuel cell and the changes due to the modifications.

The presented results clearly show that there is a significant influence of the perforation approach on the water management and therefore offers a great potential for optimization. Even though laser-perforation is an attractive method for the mass production, side-effects can easily result in structural changes and hydrophilic regions in the vicinity of the laser-treated regions. The side-effects are very sensitive to the laser intensity and exposure time and only small changes can cause significantly different results.

When using mechanical perforation, the side-effects could be prevented and indications for a beneficial drainage effect are observed using different experimental techniques. However, the increased oxygen diffusivity by the reduced saturation in the vicinity of the holes does not provide the expected impact on the cell performance. Rather, indications are found that the liquid water in the interface between the catalyst layer and the MPL is the most limiting for the oxygen diffusivity. Perforations drain this interfacial water but in drying conditions the exposed MEA results in dehydration of the MEA. Therefore, removing only the MPL in confined locations revealed the best performance both at drying and flooding conditions. The regions with the removed MPL retain the water in the MEA at drying conditions and drain the interfacial water at flooding conditions. With the reported results further improvements can be achieved by adopting the modification techniques.

Acknowledgments

The authors would like to thank the German Federal Ministry of Education and Research for the funding of the presented work in the German-Canadian cooperation project PEM-Ca-D, contract No. 03SF0360A.

Appendix A. Thermal perforation model

For estimating the effect of locally removing the PTL on the thermal management, we used a simple 3D thermal model. The model consists of the cathode CL, MPL, FS, two lands and a hole with varying diameter centered in the channel. The heat is produced in the catalyst layer due to joule and reaction heating and conducted over the PTL and the gas distribution plates where an isothermal boundary condition is applied. Table A.3 summarizes the simulation parameters. Fig. A.15 shows the dependency of the temperature lift in the perforation center and the capillary pressure on the perforation diameter.

Table A.3
Model settings and results for the estimation of the maximum temperature in the hole T_{max} and capillary pressure c_p in different hole sizes.

Thermal conductivity (membrane/CL/PTL/land)	W m^{-1} K^{-1}	0.29 [37]/0.27 [37]/10 [37]/52 [38]
Electrical conductivity (CL/PTL)	S m^{-1}	114 [39]/1958 [40]
Layer thickness (membrane/CL/PTL/land)/channel width	μm	15/5/150/200/1000
Heat production in electrode (d_{CL} = thickness CL)	W	$\frac{I_c}{d_{CL}} \cdot (0.95\ \text{V} - I_c \cdot 0.1\ \Omega - V_c)$
I_c/V_c		1.6 A cm^{-2}/0.6 V
Boundary condition: temperature/voltage in channel		340 K/V_c

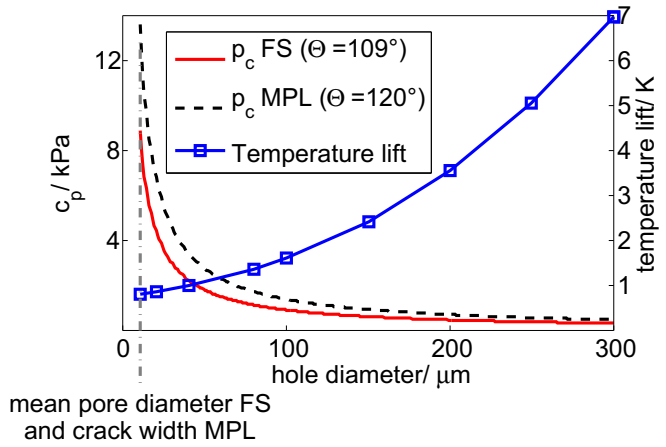


Fig. A.15. Capillary pressure p_c for the mean contact angles of the FS ($\phi = 109°$ [33]) and MPL ($\phi = 109°$ [41]) and temperature lift dependent on hole diameter in the PTL according to the thermal model.

References

[1] S. Vengatesan, M.W. Fowler, X.-Z. Yuan, H. Wang, Journal of Power Sources 196 (2011) 5045–5052.
[2] J. Wu, X.Z. Yuan, J.J. Martin, H. Wang, J. Zhang, J. Shen, S. Wu, W. Merida, Journal of Power Sources 184 (2008) 104–119.
[3] R. Borup, J. Meyers, B. Pivovar, Y.S. Kim, R. Mukundan, N. Garland, D. Myers, M. Wilson, F. Garzon, D. Wood, Chemical Reviews 107 (2007) 3904–3951.
[4] K. Seidenberger, F. Wilhelm, T. Schmitt, W. Lehnert, J. Scholta, Journal of Power Sources 196 (2011) 5317–5324.
[5] G.G. Park, Y.J. Sohn, T.H. Yang, Y.G. Yoon, W.Y. Lee, C.S. Kim, Journal of Power Sources 131 (2004) 182–187.
[6] S. Park, B.N. Popov, Fuel 88 (2009) 2068–2073.
[7] S. Park, B.N. Popov, Fuel 90 (2011) 436–440.
[8] G.Y. Lin, T. Van Nguyen, Journal of the Electrochemical Society 152 (2005) A1942–A1948.
[9] J.-C. Tsai, C.-K. Lin, Journal of the Taiwan Institute of Chemical Engineers 42 (2011) 945–951.
[10] D. Gerteisen, T. Heilmann, C. Ziegler, Journal of Power Sources 177 (2008) 348–354.
[11] D. Gerteisen, C. Sadeler, Journal of Power Sources 195 (2010) 5252–5257.
[12] K. Tüber, D. Pócza, C. Hebling, Journal of Power Sources 124 (2003) 403–414.
[13] S. Litster, D. Sinton, N. Djilali, Journal of Power Sources 154 (2006) 95–105.
[14] R. Alink, D. Gerteisen, W. Mérida, Fuel Cells 11 (2011) 481–488.
[15] A. Arvay, E. Yli-Rantala, C.H. Liu, X.H. Peng, P. Koski, L. Cindrella, P. Kauranen, P.M. Wilde, A.M. Kannan, Journal of Power Sources 213 (2012) 317–337.
[16] R. Kuhn, J. Scholta, P. Krüger, C. Hartnig, W. Lehnert, T. Arlt, I. Manke, Journal of Power Sources 196 (2011) 5231–5239.
[17] I. Manke, C. Hartnig, M. Grunerbel, W. Lehnert, N. Kardjilov, A. Haibel, A. Hilger, J. Banhart, H. Riesemeier, Applied Physics Letters 90 (2007).
[18] I. Manke, H. Markoetter, C. Toetzke, N. Kardjilov, R. Grothausmann, M. Dawson, C. Hartnig, S. Haas, D. Thomas, A. Hoell, C. Genzel, J. Banhart, Advanced Engineering Materials 13 (2011) 712–729.
[19] N. Kardjilov, I. Manke, A. Hilger, M. Strobl, J. Banhart, Materials Today 14 (2011) 248–256.
[20] M.P. Manahan, M.C. Hatzell, E.C. Kumbur, M.M. Mench, Journal of Power Sources 196 (2011) 5573–5582.
[21] M.P. Manahan, M.M. Mench, Journal of the Electrochemical Society 159 (2012) F322–F330.
[22] M. Manahan, M. Mench, ECS Transactions 41 (2011) 569–581.
[23] L. Chen, T.-F. Cao, Z.-H. Li, Y.-L. He, W.-Q. Tao, International Journal of Hydrogen Energy 37 (2012) 9155–9170.
[24] K. Nishida, T. Murakami, S. Tsushima, S. Hirai, Journal of Power Sources 195 (2010) 3365–3373.
[25] S.D. Knights, K.M. Colbow, J. St-Pierre, D.P. Wilkinson, Journal of Power Sources 127 (2004) 127–134.
[26] A. Rack, S. Zabler, B.R. Müller, H. Riesemeier, G. Weidemann, A. Lange, J. Goebbels, M. Hentschel, W. Goerner, Nuclear Instruments and Methods in Physics Research Section A: Accelerators, Spectrometers, Detectors and Associated Equipment 586 (2008) 327–344.
[27] W. Goerner, M.P. Hentschel, B.R. Müller, H. Riesemeier, M. Krumrey, G. Ulm, W. Diete, U. Klein, R. Frahm, Nuclear Instruments and Methods in Physics Research Section A: Accelerators, Spectrometers, Detectors and Associated Equipment 467–468 (Part 1) (2001) 703–706.
[28] H. Markoetter, R. Alink, J. Haußmann, K. Dittmann, T. Arlt, F. Wieder, C. Toetzke, M. Klages, C. Reiter, H. Riesemeier, J. Scholta, D. Gerteisen, J. Banhart, I. Manke, International Journal of Hydrogen Energy 37 (2012) 7757–7761.
[29] O. Herrera, D. Wilkinson, W. Merida, Journal of Power Sources 198 (2012) 132–142.
[30] D. Gerteisen, W. Merida, T. Kurz, P. Lupotto, M. Schwager, C. Hebling, Fuel Cells 11 (2011) 339–349.
[31] D. Gerteisen, N. Zamel, C. Sadeler, F. Geiger, V. Ludwig, C. Hebling, International Journal of Hydrogen Energy 37 (2012) 7736–7744.
[32] J.T. Gostick, M.A. Ioannidis, M.W. Fowler, M.D. Pritzker, Journal of Power Sources 194 (2009) 433–444.
[33] D.L. Wood III, C. Rulison, R.L. Borup, Journal of the Electrochemical Society 157 (2010) B195–B206.
[34] Y. Ji, G. Luo, C.-Y. Wang, Journal of the Electrochemical Society 157 (2010) B1753–B1761.
[35] Z. Lu, M.M. Daino, C. Rath, S.G. Kandlikar, International Journal of Hydrogen Energy 35 (2010) 4222–4233.
[36] H. Markoetter, I. Manke, P. Krger, T. Arlt, J. Haussmann, M. Klages, H. Riesemeier, C. Hartnig, J. Scholta, J. Banhart, Electrochemistry Communications 13 (2011) 1001–1004.
[37] G. He, Y. Yamazaki, A. Abudula, Journal of Power Sources 195 (2010) 1551–1560.
[38] P. Argyropoulos, K. Scott, W.M. Taama, Journal of Power Sources 79 (1999) 184–198.
[39] H. Wu, X. Li, P. Berg, International Journal of Hydrogen Energy 32 (2007) 2022–2031.
[40] SGL, Datasheet online http://www.sglgroup.com, Generic Data Sheet GDL 25 BC.pdf, 17 September 2012.
[41] J.H. Nam, M. Kaviany, International Journal of Heat and Mass Transfer 46 (2003) 4595–4611.